

Quantifying the local Li-ion diffusion over the grain boundaries of a protective coating, revealing the impact on the macroscopic Li-ion transport in an all-solid-state battery

Ming Liu

Delft University of Technology

Chao Wang

Delft University of Technology

Chenglong Zhao

Chinese Academy of Sciences <https://orcid.org/0000-0003-0286-8156>

Eveline van der Maas

Delft University of Technology

Kui Lin

Tsinghua Shenzhen International Graduate School

Violetta A. Arszelewska

Department of Radiation Science and Technology, Delft University of Technology

Baohua Li

Tsinghua Shenzhen International Graduate School

Swapna Ganapathy

Department of Radiation Science and Technology, Delft University of Technology

<https://orcid.org/0000-0001-5265-1663>

Marnix Wagemaker (✉ m.wagemaker@tudelft.nl)

Department of Radiation Science and Technology, Delft University of Technology

<https://orcid.org/0000-0003-3851-1044>

Article

Keywords: Grain boundary diffusion, Li-ion diffusion, Protective coatings, Solid-state battery, Solid-state nuclear magnetic resonance, Micron-sized solid electrolyte, Sulfur electrode

Posted Date: March 23rd, 2021

DOI: <https://doi.org/10.21203/rs.3.rs-309949/v1>

License:  This work is licensed under a Creative Commons Attribution 4.0 International License.

[Read Full License](#)

Version of Record: A version of this preprint was published at Nature Communications on October 12th, 2021. See the published version at <https://doi.org/10.1038/s41467-021-26190-2>.

Abstract

The key challenge for solid-state-batteries is to design electrode-electrolyte interfaces that combine (electro)chemical and mechanical stability with facile Li-ion transport. Typically, this presents conflicting demands, the solid electrolyte-electrode interface-area should be maximized to facilitate high currents, while it should be minimized to reduce the parasitic interface reactions and enhance stability. Addressing these issues would greatly benefit from establishing the impact of interface coatings on local Li-ion transport over the grain boundaries. Here, the three-phase Li-ion transport, between solid electrolyte, coating and electrode is revealed using exchange-NMR, disentangling the detailed quantitative impact of the coating on the Li-ion transport in solid state batteries. A Li_2S cathode is coated by LiI , providing a ductile and conductive interface with the argyrodite-sulfur electrolyte, where the exchange-NMR demonstrates that this enhances the interface transport to such an extent that the commonly applied nanosizing of the cathodic mixture can be abandoned. This leads to facile sulfur activation, preventing solid-electrolyte decomposition, in micron-sized cathodic mixtures, that can be related to the role of coatings on the Li-ion transport, providing perspectives for sulfur based solid-state-batteries.

1. Introduction

All-solid-state lithium(Li)-ion batteries are promising candidates for next-generation high energy density and safe energy storage technology¹⁻². As a liquid free system, it generally does not suffer from leakage and gas generation and the risk of a thermal runaway, inherent to liquid electrolytes used in conventional Li-ion batteries³⁻⁷. As a result, research has intensified towards solid electrolytes that display conductivities approaching, or even exceeding that of liquid electrolytes, including structural families such as LISICON, argyrodites, garnets, and NASICON-type structures^{6, 8-10}.

A major obstacle for solid state batteries is the high internal resistance for Li^+ transfer over the solid-solid electrode-electrolyte interface¹¹⁻¹² which may be due to poorly conducting electrolyte decomposition products^{4, 13}, contact loss due to volumetric changes^{4, 14} and space-charges¹⁵⁻¹⁶. The commonly applied strategy to lower the resistance for Li^+ charge transport, is to enlarge the electrolyte-electrode interface area, often expressed as “ionic contact area”, by nanosizing the electrode and electrolyte particles¹⁷⁻¹⁹. However, with the interface area between electrolyte and electrode, also scale the detrimental chemical and electrochemical reactions at the interfaces between the electrolyte and electrode, raising the internal resistance for Li^+ transport. Thus, from the perspective of stability, larger electrolyte and electrolyte particles in the micron range are preferred, having the additional advantage of being more suitable for practical production²⁰. However, this puts even higher demands on improving the Li^+ transport over the relatively small ionic contact area between micron sized solid electrolyte-electrode particles.

To address both stability and Li^+ charge transport at the interfaces has lead through the development of interphases, often realized through coating processes^{6, 18-19}. The demands on these interphases are challenging, including (electro)chemical stability towards both electrode and electrolyte, poor electronic

conductivity and at least reasonable ion conductivity, and a low grain boundary resistance with both solid electrode and electrolyte. This is typically achieved by good wettability (low interface energy) towards electrode and electrolyte and by soft interphase materials (low Young's modulus and/or yield point). One of the challenges is to assess the impact of interphases on the local Li⁺ charge transport, which can provide valuable insights for interphase design and preparation methodologies. Where the macroscopic charge transfer resistance is most often estimated by electrochemical impedance spectroscopy²¹⁻²², disentangling the three-phase diffusion between the electrode, interphase/coating and electrolyte is yet to be accomplished.

One of the solid electrolyte-electrode combinations where interphase strategies are intensively investigated is sulfur based solid electrolytes in combination with sulfur cathodes, providing a high energy density in combination with cheap raw materials and synthesis. Sulfide-based electrolytes (such as Li₂S-P₂S₅ and Li₆PS₅X (X=Cl, Br and I)) are especially promising due to their high ionic conductivity and relatively low grain boundary resistance²³⁻²⁶. These advantages, unfortunately, come along with a major drawback, which is the very small electrochemical stability window^{13, 27-28}. This is one of the main reasons for the extremely sluggish Li⁺ transport over the solid-solid Li₂S-solid electrolyte interface during battery operation, especially when micron sized solid electrolyte particles are used^{3-4, 29-31}. An additional challenge is the activation of solid sulfur cathodes due to the very low Li⁺ diffusivity³²⁻³⁴, which also demands a relatively large ionic contact area³⁵. To improve the Li⁺ interfacial transport two applied strategies are bilayer solid electrolytes design (porous layer and dense layer)^{30, 36-37} and mixing in binary lithium halide salts (such as LiBr, Lil) additives^{29-31, 38-40}. Because of the large cost and sophisticated process associated with the former, halide salt addition appears especially promising for practical application. The lower internal resistance of these three-phase mixtures has argued to be the result of the small Young's modulus (softness) of the halide salts, which effectively act as a solid wetting agent for the electrode/electrolyte interface^{29-31, 38-40}. However, how the halogen salt affects the local Li⁺ transport over the grain boundaries (electrolyte-halogen salt, halogen salt-electrode and electrolyte-electrode) is difficult to establish, and especially important to develop fundamental understanding and guide the design of the optimal design and preparation of these interphases.

Making use of the ability of solid state nuclear magnetic resonance (NMR) to characterize the spontaneous Li⁺ exchange between solid electrolyte and electrode phases in solid state cathodes⁴¹⁻⁴², the present work explores the three-phase Li⁺ transport between the Li₂S electrode, Lil coating and argyrodite Li₆PS₅Cl solid electrolyte, aiming to gain insight in the role of the coating in Li-ion transport in solid-state batteries. The difference in NMR chemical shift of the three phases allows to unravel the diffusivity between each phase via ⁶Li 2D-EXSY exchange experiments. The sluggish Li⁺ diffusion over the Li₂S-argyrodite interface is drastically improved by the presence of the Lil coating, where the Li⁺ diffusion is shown to proceed through the Lil coating. The activation energy between the three phases is equal to the bulk activation energy for Li⁺ diffusion in Lil, demonstrating the extremely low grain boundary resistance achieved by the facile Lil coating strategy. The practical consequence during battery operation is that this

prevents large overpotentials during battery cycling, even at a relatively low ionic contact area between the cathode and microscopic solid electrolyte particles. This is fortuitous, as it makes the working potential fall within the electrochemical stability of the argyrodite solid electrolyte. The result is a solid-state battery that can be activated at a very low applied voltage, and can cycle with high reversibility under a modest 2 MPa pressure for over 200 cycles. The ability to monitor the local Li⁺ transport over the grain boundaries in this three-phase system provides valuable insight in the role of coatings in achieving low interphase resistances using micron sized solid electrolyte particles, guiding the design of stable high-performance interphases, which are crucial aspects for future solid-state batteries.

2. Methods

2.1. Solid electrolyte and cathode active materials preparation.

The solid-state electrolyte Li₆PS₅Cl (denoted as LPSC) was prepared by a simple solid-state reaction. The stoichiometric raw materials LiCl (Sigma-Aldrich), P₂S₅ (Sigma-Aldrich), and Li₂S (Sigma-Aldrich) were used as the starting materials and were ball milled at 110 rpm, 2hrs with the ZrO₂ coated jars using 18 ZrO₂ balls. After the ball milling, the precursor was sealed in a quartz tube with Ar and then annealed at 550 °C for 15 hours to obtain the LPSC solid electrolyte. These were subsequently crushed with an agate mortar-pestle before using the samples for further measurements. For preparation of the Li₂S-LiI mixtures, proportional 10 mmol Li₂S and 3.33 mmol LiI were dissolved into 1 ml ethanol and stirred for 10 mins then heated at 300 °C until totally dry.

2.2. Material characterization.

Powder X-ray diffraction (XRD) patterns were collected over a two-theta range of 10–80° to identify the crystalline phases of the prepared materials using CuKα X-rays (1.5406 Å at 45 kV and 40 mA) on an X'Pert Pro X-ray diffractometer (PANalytical). To prevent reaction with moisture and oxygen, the powder materials were sealed in an airtight XRD sample holder in an argon-filled glove box. For the TEM and energy dispersive X-ray (STEM-EDX) investigations, a suspension in dry ethanol was prepared, which was drop casted onto a standard gold grid with a holey carbon film under a high temperature, inside an argon-filled glove box. To prevent any contact with air TEM grids with the sample were loaded into a custom-made vacuum transfer TEM holder. TEM measurements were carried out in a FEI-Tecnai operating at 200 kV. FE-SEM (JEOL JSM-6010LA) images were taken under dry Argon conditions, and taken using an accelerating voltage of 10 kV. The depth-profiling sputtering was conducted by 2 min of sputtering in five cycles (2 kV, 2 mm × 2 mm), the narrow spectra of particular elements were recorded after each cycle of sputtering. The pass energy used for the hemispheric analyzer was 58.7 eV, and the base pressure of the system was ~1 × 10⁻⁷ Pa. The estimated sputtering rates are 5 nm/min.

2.3. Solid-state lithium battery preparation and electrochemical performance.

Solid state cells were assembled in an argon-filled glove box in the following steps: 88 mg of LPSC was pressed relative tightly under hand pressure as the electrolyte layer, and subsequently 12.5 mg of cathode mixture and In-Li foil were brought into contact to the top and bottom faces of the solid electrolyte pallet. After that, 2 MPa pressure was applied to press these three layers together for 30 s. The assembled cells were charged and discharged under specific current densities to evaluate their electrochemical performances.

2.4. Solid-state ^6Li NMR measurements.

Solid state NMR measurements were performed on a Bruker Ascend 500 spectrometer ($B_0 = 11.7$ T) with a NEO console operating at a ^6Li resonance frequency of 73.578 MHz. The $\pi/2$ pulse length was determined to be 3.9 μs with an RF field strength of 64 kHz. Chemical shifts were referenced with respect to a 1 M LiCl solution. A Bruker two channel MAS WVT 4 mm probe was used for all measurements. One pulse experiment was performed under MAS at a spinning speed of 10 kHz. A recycle delay of three times of T_1 was used each time. Two-dimensional exchange spectroscopy (2D-EXSY) measurements were performed for the mixture at a spinning speed of 10 kHz and at various mixing times ranging from 10 ms up to 10 s and at temperatures from 20 to 100 $^\circ\text{C}$. All 2D spectra consist of 16 scans for each of the 32 transients, each transient incremented by 8000 ms with a recycle delay of up to 5 s. Exchange between the Li_2S and LPSC phases was quantified by fitting the evolution of the cross-peak intensity as a function of T_{mix} to a 3D diffusion model derived from Fick's law, which has been described previously^{4, 24}.

3. Results And Discussion

3.1. Stability of solid electrolytes, nanosized versus micronsized

The electrochemical stability of solid electrolytes was recently shown to be significantly lower than initially thought, especially for sulfide based solid electrolytes, where consequential decomposition reactions have been shown to have large detrimental impact on the all-solid-state battery performance^{10, 43-44}. To demonstrate the redox activity of the sulfur solid electrolyte material and the impact of particle size, several mixtures of sulfur solid electrolytes with carbon are galvanostatically cycled. As shown in **Figure 1a** and **b**, when nanosized Li_3PS_4 ($n\text{LPS}$) and $\text{Li}_6\text{PS}_5\text{Cl}$ ($n\text{LPSC}$) are mixed with conductive carbon (referred to as $n\text{LPS-C}$ and $n\text{LPSC-C}$ respectively), they are readily oxidized at low oxidation potentials, <2 V vs. In (<2.62 V vs. Li/Li $^+$), at a relatively low current density of 0.033 mA/cm 2 , in agreement with recent findings^{10, 25}. This illustrates that the decomposition of nanosized solid electrolytes in cathodic mixtures is the prime reason for the short cycle life of current all-solid-state batteries utilizing sulfide solid electrolytes²⁵. The combination of a Li_2S cathode and the LPSC electrolyte has been intensively studied^{3-4, 29-30}, where the harsh activation process of Li_2S , caused by the low bulk conductivity of Li_2S , and sluggish Li $^+$ transport between the electrode and electrolyte represent another critical issue. A straightforward approach to achieve easier activation of Li_2S and to improve the Li $^+$ transport between the electrode and electrolyte is to reduce the particle size of both the Li_2S and the LPSC (here referred to

as $n\text{Li}_2\text{S}$ - $n\text{LPSC-C}$ electrode). Accompanied by a large overpotential of ~ 800 mV, this results in a substantial capacity during first charge and discharge and upon subsequent cycling, as shown in **Figure 1f** and **Figure S1**, which is however hard to distinguish from the capacity of the electrolyte itself (because oxidation of LPSC is carried by the S^{2-}/S redox).

The simplest strategy to reduce the contribution of the solid electrolyte to the capacity is to lower the ionic contact area through the use of micron sized solid electrolyte particles. To verify the smaller redox activity, micron sized LPSC (average diameter of 50 nm, as shown in **Figure S2**) was mixed with carbon, and charged (oxidized) to 3 V vs. In-Li (3.62 vs. Li/Li $^+$) in the solid-state battery configuration, referred to as the $m\text{LPSC-C}$ electrode. The result, shown in **Figure 1c**, demonstrates nearly no contribution of the LPSC solid electrolyte to the capacity, reflecting the smaller amount of decomposition reactions under the same current density. However, as expected, the small ionic contact area of micron sized LPSC compromises ion transport over the interface, leading to a very small capacity of the sulfur active material, even when nanosized Li_2S is employed as shown in **Figure 1d**. Although nanosized Li_2S displays a slightly larger capacity, the rapid voltage increases to the 3.5 V vs. In-Li (4.12 vs. Li/Li $^+$) cut-off demonstrates that in both cases the sulfur cathode material is marginally activated. At the same time, decreasing the ionic contact area increases the internal resistance and thus the overpotentials experienced at the solid electrolyte, which will induce decomposition reactions and thus driving a self-amplifying resistance growth towards battery failure.

The mechanical mixing of halogen salts like LiI with Li_2S and sulfide solid electrolytes is an often-applied strategy, to improve conductivity, although the exact mechanism has not been clarified^{29-31, 38-39}. At present we take a different and more controlled approach to study the detailed impact of LiI on the Li-ion transport over the grain boundaries by NMR exchange experiments, and introduce LiI at the Li_2S -LPSC interfaces. Rather than using the conventional ball-milling route, this is achieved by introducing LiI via solution, making use of the much better solubility of LiI in ethanol compared to Li_2S (see supporting information **Figure S3**). The solution was then evaporated at 300 °C (**Figure S3**) to obtain a $\text{LiI-Li}_2\text{S}$ (1:3 molar ratio) composite, where LiI precipitates on the surface of Li_2S as discussed below. This cathode was subsequently hand mixed with LPSC and C (referred to $m\text{Li}_2\text{S(LiI)}$ - $m\text{LPSC-C}$) to prepare the cathodic mixture and an all-solid-state $m\text{Li}_2\text{S(LiI)}$ - $m\text{LPSC-C}$ | $m\text{LPSC}$ |In-Li battery was assembled under 2 MPa pressure. This has a large impact on the electrochemical charging, as shown in **Figure 1e**, demonstrating that the introduction of LiI results in a very low sulfur redox activation plateau at 1.69 V vs. In (2.31 V vs. Li/Li $^+$) of the micron sized Li_2S combined with micron sized LPSC. The plateau is followed by a rapid increase in potential which reflects oxidation of the solid electrolyte and/or of LiI (to LiI_3 which is known to occur at ~ 2.3 V vs. In)⁴⁵⁻⁴⁶. To identify the contribution of the LiI and/or LPSC oxidation, this measurement was repeated in a battery without Li_2S , shown in **Figure 1e**, leading to charging at a higher voltage marking the oxidation of LPSC and/or LiI . In conclusion, deposition of LiI on Li_2S via solution, and hand mixing this cathode with LPSC results in an extremely low activation (oxidation) potential for

Li_2S , suggesting that facile Li^+ transport between the electrode and electrolyte is achieved even for a relatively small ionic contact area between the micronsized solid electrolyte and the electrode particles.

3.2. Electrode and LiI coating synthesis and characterization

To understand the role of LiI in the activation of Li_2S , a detailed structural investigation was performed. Both LiI and Li_2S have a cubic structure indexed to the $\text{Fd}-3\text{m}$ space group. Three $\text{Li}_2\text{S}-\text{LiI}$ composites were prepared via dissolution and precipitation where $\text{Li}_2\text{S}:\text{LiI}$ molar ratios of 9:1, 3:1, and 1:1 were added to ethanol, followed by evaporation of the solution at 300 °C. Li_2S and LiI were also individually dissolved and precipitated from ethanol via evaporation for comparison. X-ray patterns of pristine Li_2S and LiI precipitated Li_2S and LiI and the three $\text{Li}_2\text{S}-\text{LiI}$ composites are provided in **Figure 2a** and **S4**. From a cursory inspection it can be observed that the peaks corresponding to the precipitated Li_2S are much broader than those of the parent Li_2S , while the peak width of precipitated LiI is comparable to the parent LiI . This indicates that on precipitation smaller primary crystallites of Li_2S are obtained. In the three composite mixtures, both the Li_2S and LiI phases could be indexed, albeit with shifts in peak positions of the Li_2S component indicating changes in lattice parameters of this phase. Rietveld refinement was further performed of all the patterns depicted in **Figure S5**, and the lattice parameters obtained from the refinement are given in **Figure S4**. It can be seen that the lattice parameter of LiI (6.025 Å) remains unchanged from that of the pristine material. On the other hand, with increasing amounts of LiI in the composite the lattice parameter of Li_2S keeps increasing from 5.701 Å (pristine) to 5.750 Å (1 $\text{Li}_2\text{S}:1\text{LiI}$), which could be due to the much smaller average crystallite size of 9.18 nm (1 $\text{Li}_2\text{S}:1\text{LiI}$) compared to 162.92 nm (pristine) as shown in **Figure S6** or by incorporation of the I in the Li_2S lattice.

Additional SEM and TEM measurements are performed to study the morphology of the pristine Li_2S and the $\text{Li}_2\text{S}-\text{LiI}$ mixture. As shown in **Figure 2c**, the prepared mixture consists of a microstructure comprising of micron sized secondary particles with a relatively uniform particle size of around 5 mm similar to pristine Li_2S in **Figure 2b**. TEM is used to study the morphology at smaller length scales (100 nm). As seen from the TEM image and energy spectrum (**Figure 2d**), the EDS mapping of the particle surface shows uniform S and I distribution, indicating a mixture on the nanoscale was obtained with this precipitation method, and the LiI was uniformly distributed over the surface structure of Li_2S particles. To further verify the structure of the $\text{Li}_2\text{S}-\text{LiI}$ material, XPS depth profiling was performed as shown in **Figure 2e and f**. The S 2p XPS signal is relatively low until a depth of ~100 nm, and vice versa the I 3d is relatively high to approximately the same depth (selected window diameter is as small as 14 nm to locate only a few particles). Therefore, the present precipitation method results in micron sized secondary cathode particles, referred to as $\text{mLi}_2\text{S}(\text{LiI})$, that exist of agglomerates of LiI coated nanosized primary Li_2S particles, where the micron sized agglomerates are coated by a relatively thick LiI layer at some positions accumulating to large domains of LiI (as observed with XRD).

3.3. Li-ion conductivity and role of LiI in the Li-ion transport mechanism

To investigate the impact of the Lil coating on the conductivity, impedance spectroscopy and ${}^6\text{Li}$ solid NMR spectroscopy experiments are conducted. The temperature dependence of the ionic conductivities for the pristine Li_2S and Lil as well as pellets of the 3:1 Li_2S -Lil composite are presented in **Figure 3a**. The conductivity of all the materials follow an Arrhenius law, resulting in activation energies of 0.235, 0.107 and 0.212 eV for Li_2S , Lil and the Li_2S -Lil mixture, respectively. The room-temperature conductivity of the Li_2S -Lil mixture ($6.72 \times 10^{-9} \text{ S/cm}$ at 25°C) is between that of Li_2S ($7.51 \times 10^{-11} \text{ S/cm}$ at 25°C) and Lil ($0.97 \times 10^{-7} \text{ S/cm}$ at 25°C), indicating that the Lil in the Li_2S agglomerates enhances the overall conductivity of the cathode material. To investigate the role of Lil as interphase material between the Li_2S electrode and LPSC solid electrolyte, (2D) ${}^6\text{Li}$ - ${}^6\text{Li}$ exchange (2D-EXSY) solid state NMR experiments are performed. These experiments can provide selective and non-invasive quantification of the spontaneous Li^+ diffusion, charge transfer, over the solid–solid electrolyte–electrode interface (between two phases) in realistic solid state cathode mixtures, as previously reported^{4,24}. The one-dimensional (1D) ${}^6\text{Li}$ magic angle spinning (MAS) NMR spectra of the micron sized Li_2S -LPSC cathode mixture, shown in **Figure 3b**, displays two resonances with chemical shifts of 2.31 and 1.29 ppm, representing Li in Li_2S and in LPSC respectively. Compared to Li_2S , the larger screening of Li^+ in the LPSC results in the upfield ${}^6\text{Li}$ chemical shift position. The difference in chemical shift between Li in Li_2S and LPSC that allows to distinguish both species, makes it possible to conduct the 2D exchange experiments. In the 2D exchange spectrum, **Figure 3c**, both Li^+ environments observed in the 1D spectra are clearly observed, where the more LPSC narrow resonance is due to the higher mobility of Li^+ in the solid electrolyte. 2D exchange NMR effectively measures the spectrum of the ${}^6\text{Li}$ ions at $t=0$ s, then waits a mixing time T_{mix} and subsequently measure the spectrum of the same ions again at $t=T_{mix}$. Li^+ diffusion over the grain boundaries between the two chemical Li environments (Li_2S and in LPSC) should result in off-diagonal cross-peaks, positioned in the dotted boxes in **Figure 3c**. The intensity of these cross-peaks reflects the amount of Li^+ exchange, which is expected to increase when the diffusion time (T_{mix}) and temperature are increased⁴. The absence of off-diagonal intensity, even for the maximum T_{mix} and temperature ($T_{mix}= 20\text{s}, 373\text{K}$) indicates that the Li^+ exchange (flux) over the solid–solid interface between LPSC and Li_2S (without Lil coating), is too small to be observed, reflecting sluggish Li^+ mobility across the interface with the solid electrolyte. This rationalizes the observation in **Figure 1d**, that these mixtures do not facilitate activation of Li_2S . As expected, the addition of Lil to the cathodic mixture, $m\text{Li}_2\text{S}(\text{Lil})$ - $m\text{LPSC}$, results in the appearance of the Li resonance at -4.56 ppm associated with Lil, in the 1D ${}^6\text{Li}$ NMR spectrum (**Figure 3d**). The impact of the Lil on the spontaneous Li^+ charge transfer, between Li_2S and LPSC is dramatic, as can be observed in **Figure 3e-i**. At short mixing time, $T_{mix} = 10 \text{ ms}$, no appreciable cross-peak intensity is observed in the 2D EXSY spectrum (**Figure 3g**). However, increasing the mixing time, T_{mix} to 10 s, and raising the temperature to 373 K, results in a strong cross-peak intensity (**Figure 3h and i**), which is a measure of the Li^+ exchange between Li_2S and LPSC. The evolution of the normalized cross-peak intensity as a function of T_{mix} measured at a range of temperatures and a T_{mix} range of 10 ms-10 s is provided in **Figure 3e**. Exchange

between the Li_2S and LPSC phases was quantified by fitting the evolution of the cross-peak intensity as a function of T_{mix} to a diffusion model derived from Fick's law, described elsewhere²⁴. From the fit, the diffusion coefficient (D) as a function of temperature can be obtained, which in this case pertains to Li-ion transport across the Li_2S -LPSC interface. The diffusion coefficients as a function of temperature obtained from the fit are given in **Figure 3f**. The data for Li_2S -LPSC diffusion can be fit to an Arrhenius law, yielding an activation energy of 0.107 eV for the charge transfer. This activation energy equals that of Lil as measured by impedance of the pure phase, suggesting that Lil is responsible for lowering the interfacial barrier between electrode and electrolyte. The value for the activation energy and observed Li^+ exchange is comparable to that obtained for interfacial diffusion between nanosized Li_2S and nanosized (average particle size ~ 100 nm) LPSC argyrodite (0.10-0.13 eV)³⁻⁴. The remarkable conclusion is that, despite the small ionic contact area of the present micron sized LPSC (average particle size $\sim 50 \mu\text{m}$) in the cathodic mixtures, the interface transport is improved to such an extent that it matches that of nanostructured mixtures having a much large ionic contact area. The two orders of magnitude difference in diameter between the LPSC in the cathodic mixtures, suggests that the Lil improves the Li^+ diffusion over the interface with 4 orders of magnitude.

To understand the role of the Lil in the diffusion, **Figure 4a** focuses on the exchange of Li in Li_2S and LPSC with Lil, hence the three phase Li-ion exchange in the 2D EXSY measurements shown in **Figure 3**. **Figure 4a** displays clear exchange of Li^+ between Lil and both Li_2S and LPSC, reflecting the equilibrium exchange of Li^+ between the three phases in the cathodic mixture. This represents a unique view into the charge transport between the coating and the electrode and electrolyte phases in a solid state battery. By measuring and fitting the exchange intensities as a function mixing time and temperature, **Figure 4c-f**, similar to the evaluation of the direct exchange between Li_2S and LPSC, the diffusion coefficients and activation energy over both the LPSC-Lil and Lil- Li_2S interfaces is quantified. To the best of our knowledge, this is the first quantification of the local ion diffusion between a coating and its facing solid phases, providing insight in the impact of a coating on the Li-ion transport. The high diffusivity and very low activation energies for charge transfer from Li_2S to Lil and LPSC to Lil, 0.142 eV and 0.117 eV respectively, are similar to the overall charge transfer between Li_2S and LPSC. This indicates that Lil facilitates the charge transfer and thus functions as the bridge between electrode and electrolyte as summarized schematically in **Figure 4b**. Apparently, the ductile Lil⁴⁰ creates grain boundaries between both the electrolyte and electrode material that do not pose an additional barrier for Li-ion diffusion, and the diffusivity of Lil itself dictates the diffusivity between electrode and electrolyte.

3.4. Electrochemical performance

To test the efficacy of the Li_2S -Lil cathode in combination with the micron sized LPSC, $m\text{Li}_2\text{S}(\text{Lil})$ - $m\text{LPSC-Cl}$ | $m\text{LPSC}$ |In-Li, all-solid-state batteries were assembled, during which only a mild pressure, 2MPa, was applied (see methods section for assembly details). The battery performance is shown in **Figure 5**. Although the battery can be activated during charge to over 900 mAh/g capacity as shown in **Figure 1e**,

discharge leads to large overpotentials. The increase of the oxidation potential towards 900 mAh/g exceeds the oxidation potential of LiI (2.3 V vs. In-Li) and that of the LPSC electrolyte (2.1 V vs. In-Li), which will result in poorly conducting species near the interfaces that increase the impedance. To prevent this, the battery is charged to specific capacities (fixed charge capacity) as shown in **Figure 5a**, followed by discharging to a fixed potential (0.8 V vs. In-Li) to achieve complete discharge. After the battery is initially charged to 600 mAh/g directly, the battery was cycled up to 50 cycles at different currents with an average Coulombic efficiency higher than 97.8% (**Figure 5b**). The 1st, 25th and 50th charge and discharge curves of the *m*Li₂S(LiI)-*m*LPSC-C|*m*LPSC|In-Li battery cycled at 0.132 mA/cm², shown in **Figure 5c**, demonstrate an ultra-low activation potential of 1.7 V vs. In-Li, amounting an overpotential of only ~100 mV. This is the lowest overpotential reported (**Figure 5d and Table S1**) to date and the consequence of the facile Li-ion transport induced by the LiI coating as observed by the exchange NMR experiments. Post-mortem XRD analysis after different states of charge, and NMR analysis after 50 cycles (ending in the charged state) of the cycled *m*Li₂S(LiI)-*m*LPSC-C active materials can be found in **Figure S7**. After the first charge to 600 mAh/g and even after the 50th charge to 600 mAh/g, only the Li₂S is oxidized, towards an amorphous structure, and the micron sized LPSC solid electrolyte remains intact as no decomposition products are observed⁴⁷. The long cycling stability of the battery with a higher mass loading, 6.4 mg/cm², is demonstrated in **Figure 5e**. After 200 cycles, the Coulombic efficiency maintains values exceeding 99.9% resulting in an average Coulombic efficiency of 99.6%. Most notable is that this is achieved in combination with micron sized electrolyte particles, a small ionic contact area, and that further optimization can be expected upon variation of the amount of LiI, the applied pressure, charge capacity and the cathodic mixture.

4. Conclusion

In summary, the impact of a ductile coating on the diffusion over the grain boundary between the electrode and solid electrolyte is investigated. 2D exchange NMR reveals and quantifies the spontaneous equilibrium Li⁺ between Li₂S electrode, LiI coating and argyrodite Li₆PS₅Cl solid electrolyte, thus uniquely disentangling the impact of the coating on the Li⁺ diffusion. Effectively, the ductile LiI lowers the barrier for grain boundary diffusion towards both the Li₂S (electrode) and Li₆PS₅Cl (electrolyte) phases to such an extent that the conductivity of the thin LiI coating dominates. This improves the charge transfer between electrode and electrolyte with several orders of magnitude and enables to move from nanostructured solid state cathode mixtures to micron-sized solid state cathode mixtures, the latter having the practical advantages of high stability and facile material and electrode production. The impact of the improved charge transfer is demonstrated by a sulfide based solid state battery which combines easy activation of the sulfur electrode at very low overpotentials with stable cycling. This work demonstrates the ability of exchange NMR unambiguously quantify and disentangle the Li⁺ transport over the interfaces between electrode, coating and solid electrolyte (three phase exchange) in solid state batteries. As one of the key challenges towards solid state batteries is the development of interphases to

establish stability and facile Li⁺ transport, the present approach and insights provides valuable insights to guide future understanding and material design.

Declarations

Acknowledgements

The authors thank Michel Steenvoorden, and Frans Ooms for their assistance with experiments. Financial support is greatly acknowledged from the Netherlands Organization for Scientific Research (NWO) under the VICI grant nr. 16122. Financial support from the Advanced Dutch Energy Materials (ADEM) program of the Dutch Ministry of Economic Affairs, Agriculture and Innovation is gratefully acknowledged. C.W. would like to thank the Guangzhou Elite Project for financially supporting part of the work in this paper.

Author contributions

M.W. and M.L. conceived the research and designed the experiments. M.L. and C.W. carried out materials synthesis and electrochemical characterization. C.Z., K.L., E.V.M. and S.G. participated in part of the synthesis and materials characterization. M.L. S.G. and M.W. co-wrote the paper. M.L., C.W. and C.Z. contributed equally to this work. All authors discussed the results and improved on the manuscript.

Additional information

Supplementary information is available online.

Competing interests

The authors declare no competing financial interests.

References

1. Goodenough, J. B.; Kim, Y., Challenges for rechargeable Li batteries. *Chem Mater* **2010**, *22* (3), 587-603.
2. Goodenough, J. B.; Park, K.-S., The Li-ion rechargeable battery: a perspective. *J Am Chem Soc* **2013**, *135* (4), 1167-1176.
3. Yu, C.; Ganapathy, S.; de Klerk, N. J.; Roslon, I.; van Eck, E. R.; Kentgens, A. P.; Wagemaker, M., Unravelling Li-Ion Transport from Picoseconds to Seconds: Bulk versus Interfaces in an Argyrodite Li₆PS₅Cl-Li₂S All-Solid-State Li-Ion Battery. *J Am Chem Soc* **2016**, *138* (35), 11192-201.
4. Yu, C.; Ganapathy, S.; Eck, E.; Wang, H.; Basak, S.; Li, Z.; Wagemaker, M., Accessing the bottleneck in all-solid state batteries, lithium-ion transport over the solid-electrolyte-electrode interface. *Nat Commun* **2017**, *8* (1), 1086.
5. Tian, Y. S.; Shi, T.; Richards, W. D.; Li, J. C.; Kim, J. C.; Bo, S. H.; Ceder, G., Compatibility issues between electrodes and electrolytes in solid-state batteries. *Energ Environ Sci* **2017**, *10* (5), 1150-1166.

6. Manthiram, A.; Yu, X. W.; Wang, S. F., Lithium battery chemistries enabled by solid-state electrolytes. *Nat Rev Mater* **2017**, *2* (4).
7. Kato, Y.; Hori, S.; Saito, T.; Suzuki, K.; Hirayama, M.; Mitsui, A.; Yonemura, M.; Iba, H.; Kanno, R., High-power all-solid-state batteries using sulfide superionic conductors. *Nat Energy* **2016**, *1*.
8. Cheng, X. B.; Zhao, C. Z.; Yao, Y. X.; Liu, H.; Zhang, Q., Recent Advances in Energy Chemistry between Solid-State Electrolyte and Safe Lithium-Metal Anodes. *Chem* **2019**, *5* (1), 74-96.
9. Banerjee, A.; Tang, H. M.; Wang, X. F.; Cheng, J. H.; Nguyen, H.; Zhang, M. H.; Tang, D. H. S.; Wynn, T. A.; Wu, E. A.; Doux, J. M.; Wu, T. P.; Ma, L.; Sterbinsky, G. E.; D'Souza, M. S.; Ong, S. P.; Meng, Y. S., Revealing Nanoscale Solid-Solid Interfacial Phenomena for Long-Life and High-Energy All-Solid-State Batteries. *Acs Appl Mater Inter* **2019**, *11* (46), 43138-43145.
10. Han, F. D.; Zhu, Y. Z.; He, X. F.; Mo, Y. F.; Wang, C. S., Electrochemical Stability of $\text{Li}_{10}\text{GeP}_2\text{S}_{12}$ and $\text{Li}_7\text{La}_3\text{Zr}_2\text{O}_{12}$ Solid Electrolytes. *Adv Energy Mater* **2016**, *6* (8).
11. Yan, H. F.; Wang, H. C.; Wang, D. H.; Li, X.; Gong, Z. L.; Yang, Y., In Situ Generated $\text{Li}_2\text{S-C}$ Nanocomposite for High-Capacity and Long-Life All-Solid-State Lithium Sulfur Batteries with Ultrahigh Areal Mass Loading. *Nano Letters* **2019**, *19* (5), 3280-3287.
12. Xu, R. C.; Han, F. D.; Ji, X.; Fan, X. L.; Tu, J. P.; Wang, C. S., Interface engineering of sulfide electrolytes for all-solid-state lithium batteries. *Nano Energy* **2018**, *53*, 958-966.
13. Schwietert, T. K.; Arszelewska, V. A.; Wang, C.; Yu, C.; Vasileiadis, A.; de Klerk, N. J. J.; Hageman, J.; Hupfer, T.; Kerkamm, I.; Xu, Y.; van der Maas, E.; Kelder, E. M.; Ganapathy, S.; Wagemaker, M., Clarifying the relationship between redox activity and electrochemical stability in solid electrolytes. *Nat Mater* **2020** *19*, 428-435.
14. Liu, M.; Wang, C.; Cheng, Z.; Ganapathy, S.; Haverkate, L. A.; Unnikrishnan, S.; Wagemaker, Controlling the Li-metal growth to enable low Li-metal excess all solid state Li-metal batteries. *ACS Mater Lett* **2020** *2*, 665-670.
15. de Klerk, N. J. J.; Wagemaker, M., Space-Charge Layers in All-Solid-State Batteries; Important or Negligible? *ACS Appl Energy Mater* **2018**, *1* (10), 5609-5618.
16. Swift, M. W.; Qi, Y., First-Principles Prediction of Potentials and Space-Charge Layers in All-Solid-State Batteries. *Phys Rev Lett* **2019**, *122* (16).
17. Park, J.; Kim, J. Y.; Shin, D. O.; Oh, J.; Kim, J.; Lee, M. J.; Lee, Y.-G.; Ryou, M.-H.; Lee, Y. M. Dimension-controlled solid oxide electrolytes for all-solid-state electrodes: Percolation pathways, specific contact area, and effective ionic conductivity. *Chem Engineering Journal*, **2020**, *391*, 123528.
18. Quararone, E.; Mustarelli, Electrolytes for solid-state lithium rechargeable batteries: recent advances and perspectives. *Chem Soc Rev.*, **2011**, *40* (5), 2525-2540.
19. Xu, K. Electrolytes and interphases in Li-ion batteries and beyond. *Chem Rev.*, **2014**, *114* (23), 11503-11618.
20. Liu, M.; Cheng, Z.; Ganapathy, S.; Wang, C.; Haverkate, L. A.; Tulodziecki, M.; Unnikrishnan, S.; Wagemaker, M., Tandem Interface and Bulk Li-Ion Transport in a Hybrid Solid Electrolyte with

- Microsized Active Filler. *Acs Energy Lett* **2019**, *4* (9), 2336-2342.
21. Simon, F. J.; Hanauer, M.; Henss, A.; Richter, F. H.; Janek, Interfaces, Properties of the interphase formed between argyrodite-type $\text{Li}_6\text{PS}_5\text{Cl}$ and polymer-based $\text{PEO}_{10}\text{: LiTFSI}$. *ACS app Mater Inter*; **2019**, *11* (45), 42186-42196.
22. Simon, F. J.; Hanauer, M.; Richter, F. H.; Janek, Interphase Formation of $\text{PEO}_{20}\text{: LiTFSI-Li}_6\text{PS}_5\text{Cl}$ Composite Electrolytes with Lithium Metal. *ACS Appl Mater Inter*; **2020**, *12* (10), 11713-11723.
23. de Klerk, N. J. J.; Roslon, T.; Wagemaker, M., Diffusion Mechanism of Li Argyrodite Solid Electrolytes for Li-Ion Batteries and Prediction of Optimized Halogen Doping: The Effect of Li Vacancies, Halogens, and Halogen Disorder. *Chem Mater* **2016**, *28* (21), 7955-7963.
24. Ganapathy, S.; Yu, C.; van Eck, E. R. H.; Wagemaker, M., Peeking across Grain Boundaries in a Solid-State Ionic Conductor. *Acs Energy Lett* **2019**, *4* (5), 1092-1097.
25. Tan, D. H. S.; Wu, E. A.; Nguyen, H.; Chen, Z.; Marple, M. A. T.; Doux, J. M.; Wang, X. F.; Yang, H. D.; Banerjee, A.; Meng, Y. S., Elucidating Reversible Electrochemical Redox of $\text{Li}_6\text{PS}_5\text{Cl}$ Solid Electrolyte. *Acs Energy Lett* **2019**, *4* (10), 2418-2427.
26. de Klerk, N. J. J.; van der Maas, E.; Wagemaker, M., Analysis of Diffusion in Solid-State Electrolytes through MD Simulations, Improvement of the Li-Ion Conductivity in beta- Li_3PS_4 as an Example. *ACS Appl Energy Mater* **2018**, *1* (7), 3230-3242.
27. Zhu, Y. Z.; He, X. F.; Mo, Y. F., Origin of Outstanding Stability in the Lithium Solid Electrolyte Materials: Insights from Thermodynamic Analyses Based on First-Principles Calculations. *Acs Appl Mater Inter* **2015**, *7* (42), 23685-23693.
28. Richards, W. D.; Miara, L. J.; Wang, Y.; Kim, J. C.; Ceder, G., Interface Stability in Solid-State Batteries. *Chem mater* **2016**, *28* (1), 266-273.
29. Hakari, T.; Hayashi, A.; Tatsumisago, M., Li_2S -Based Solid Solutions as Positive Electrodes with Full Utilization and Superlong Cycle Life in All-Solid-State Li/S Batteries. *Adv Sustain Syst* **2017**, *1* (6).
30. Xu, R. C.; Yue, J.; Liu, S. F.; Tu, J. P.; Han, F. D.; Liu, P.; Wang, C. S., Cathode-Supported All-Solid-State Lithium-Sulfur Batteries with High Cell-Level Energy Density. *Acs Energy Lett* **2019**, *4* (5), 1073-1079.
31. Yu, C.; Hageman, J.; Ganapathy, S.; van Eijck, L.; Zhang, L.; Adair, K. R.; Sun, X. L.; Wagemaker, M., Tailoring $\text{Li}_6\text{PS}_5\text{Br}$ ionic conductivity and understanding of its role in cathode mixtures for high performance all-solid-state Li-S batteries. *J Mater Chem A* **2019**, *7* (17), 10412-10421.
32. Han, F.; Yue, J.; Fan, X.; Gao, T.; Luo, C.; Ma, Z.; Suo, L.; Wang, C., High-Performance All-Solid-State Lithium-Sulfur Battery Enabled by a Mixed-Conductive Li_2S Nanocomposite. *Nano Lett* **2016**, *16* (7), 4521-7.
33. El-Shinawi, H.; Cussen, E. J.; Corr, S. A., A facile synthetic approach to nanostructured Li_2S cathodes for rechargeable solid-state Li-S batteries. *Nanoscale* **2019**, *11* (41), 19297-19300.
34. Wu, F. X.; Lee, J. T.; Zhao, E. B.; Zhang, B.; Yushin, G., Graphene- Li_2S -Carbon Nanocomposite for Lithium-Sulfur Batteries. *Acs Nano* **2016**, *10* (1), 1333-1340.

35. Famprikis, T.; Canepa, P.; Dawson, J. A.; Islam, M. S.; Masquelier, Fundamentals of inorganic solid-state electrolytes for batteries. *Nat Mater.* **2019**, 1-14.
36. Fu, K. K.; Gong, Y.; Dai, J.; Gong, A.; Han, X.; Yao, Y.; Wang, C.; Wang, Y.; Chen, Y.; Yan, C. Flexible, solid-state, ion-conducting membrane with 3D garnet nanofiber networks for lithium batteries. *Proceedings of the National Academy of Sciences of the United States of America* **2016**, 113 (26), 7094-7099.
37. Fu, K. K.; Gong, Y.; Hitz, G. T.; McOwen, D. W.; Li, Y.; Xu, S.; Wen, Y.; Zhang, L.; Wang, C.; Pastel, Three-dimensional bilayer garnet solid electrolyte based high energy density lithium metal–sulfur batteries. *Energy Environ Sci* **2017**, 10 (7), 1568-1575.
38. Suyama, M.; Kato, A.; Sakuda, A.; Hayashi, A.; Tatsumisago, M., Lithium dissolution/deposition behavior with Li_3PS_4 -Lil electrolyte for all-solid-state batteries operating at high temperatures. *Electrochim Acta* **2018**, 286, 158-162.
39. Han, F. D.; Yue, J.; Zhu, X. Y.; Wang, C. S., Suppressing Li Dendrite Formation in Li_2S - P_2S_5 Solid Electrolyte by Lil Incorporation. *Adv Energy Mater* **2018**, 8 (18), 1703644.
40. Singh, N.; Horwath, J. P.; Bonnick, P.; Suto, K.; Stach, E. A.; Matsunaga, T.; Muldoon, J.; Arthur, The role of lithium iodide addition to lithium thiophosphate: Implications beyond conductivity. *Chem Mater* **2020**, 32, 7150-7158.
41. Grey, C. P.; Dupre, N., NMR studies of cathode materials for lithium-ion rechargeable batteries. *Chem Rev* **2004**, 104 (10), 4493-4512.
42. Pecher, O.; Carretero-Gonzalez, J.; Griffith, K. J.; Grey, C. P., Materials' Methods: NMR in Battery Research. *Chem Mater* **2017**, 29 (1), 213-242.
43. Wenzel, S.; Sedlmaier, S. J.; Dietrich, C.; Zeier, W. G.; Janek, J., Interfacial reactivity and interphase growth of argyrodite solid electrolytes at lithium metal electrodes. *Solid State Ionics* **2018**, 318, 102-112.
44. Koerver, R.; Walther, F.; Aygun, I.; Sann, J.; Dietrich, C.; Zeier, W. G.; Janek, J., Redox-active cathode interphases in solid-state batteries. *J Mater Chem A* **2017**, 5 (43), 22750-22760.
45. Zhao, Q.; Lu, Y. Y.; Zhu, Z. Q.; Tao, Z. L.; Chen, J., Rechargeable Lithium-Iodine Batteries with Iodine/Nanoporous Carbon Cathode. *Nano Letters* **2015**, 15 (9), 5982-5987.
46. Liu, M.; Ren, Y. X.; Jiang, H. R.; Luo, C.; Kang, F. Y.; Zhao, T. S., An efficient Li_2S -based lithium-ion sulfur battery realized by a bifunctional electrolyte additive. *Nano Energy* **2017**, 40, 240-247.
47. Liu, M.; Zhou, D.; He, Y. B.; Fu, Y. Z.; Qin, X. Y.; Miao, C.; Du, H. D.; Li, B. H.; Yang, Q. H.; Lin, Z. Q.; Zhao, T. S.; Kang, F. Y., Novel gel polymer electrolyte for high-performance lithium-sulfur batteries. *Nano Energy* **2016**, 22, 278-289.

Figures

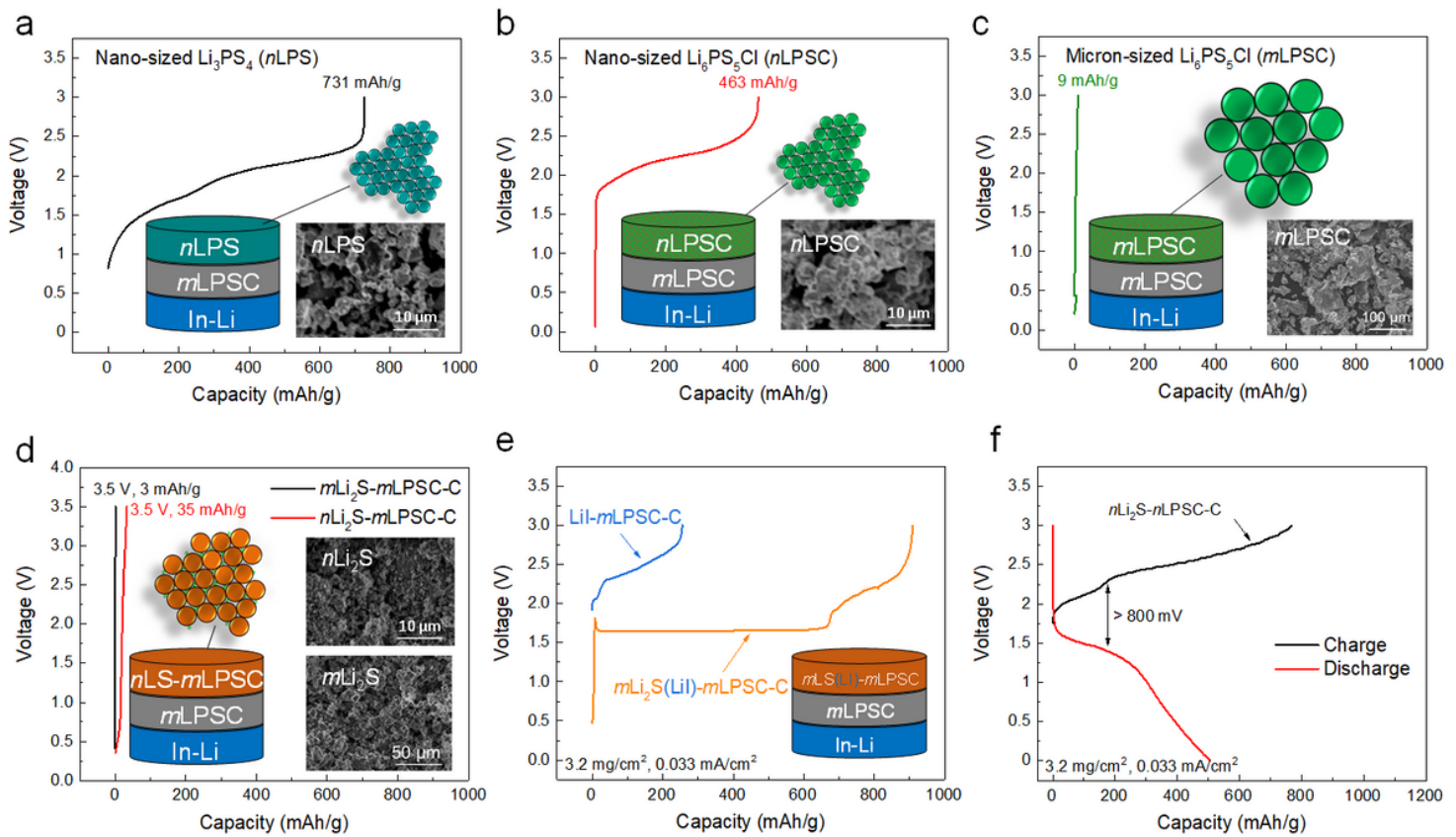


Figure 1

Electrochemical activity of nanosized and micronsized solid sulfur electrolytes and solid-state sulfur electrodes. (a-c) voltage profiles of (a) nanosized nLPS-C, (b) nLPSC-C and (c) micron sized mLPSC-C cathodes; In this configuration the solid electrolyte acts as a cathode electrode material due to the conductive carbon mixed in, which allows direct evaluation of the electrochemical activity as these would occur in a solid-state battery, excluding specific (electro)chemical reactions with a cathode material. (d) Activation voltage profiles of mLi₂S-mLPSC-C, nLi₂S-mLPSC-C cathodes; (e, f) Voltage profiles of mLi₂S(Li)-mLPSC-C, LiI-mLPSC-C and nLi₂S-nLPSC-C cathodes; For all voltage profiles the current density is 0.033 mA/cm².

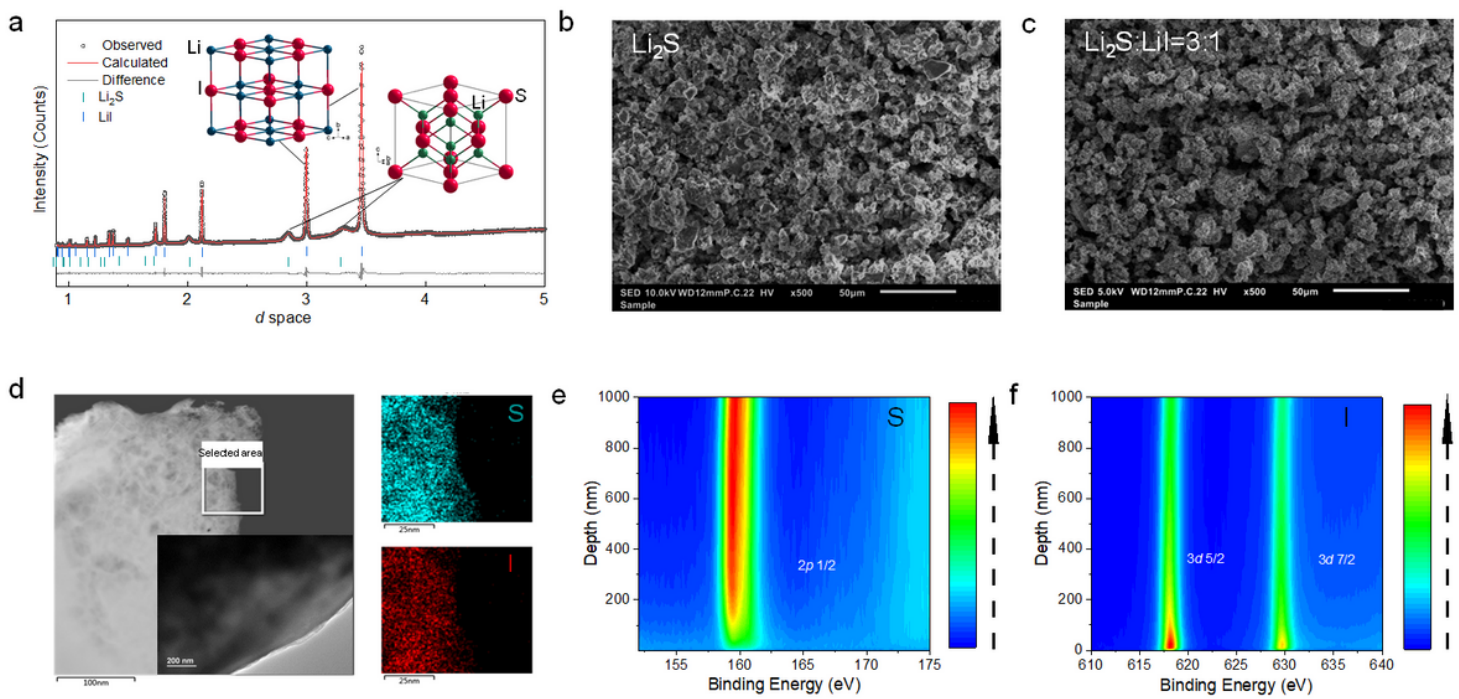


Figure 2

Structural characterizations of the active materials. (a) XRD pattern of the Li₂S-LiI materials. The pattern is fit with the Rietveld method as implemented in GSAS; (b, c, d) SEM images, TEM images and energy spectrum of the Li₂S and Li₂S-LiI (3:1) materials; (e, f) S 2p and I 3d XPS depth profiles of the pristine Li₂S-LiI (3:1) materials.

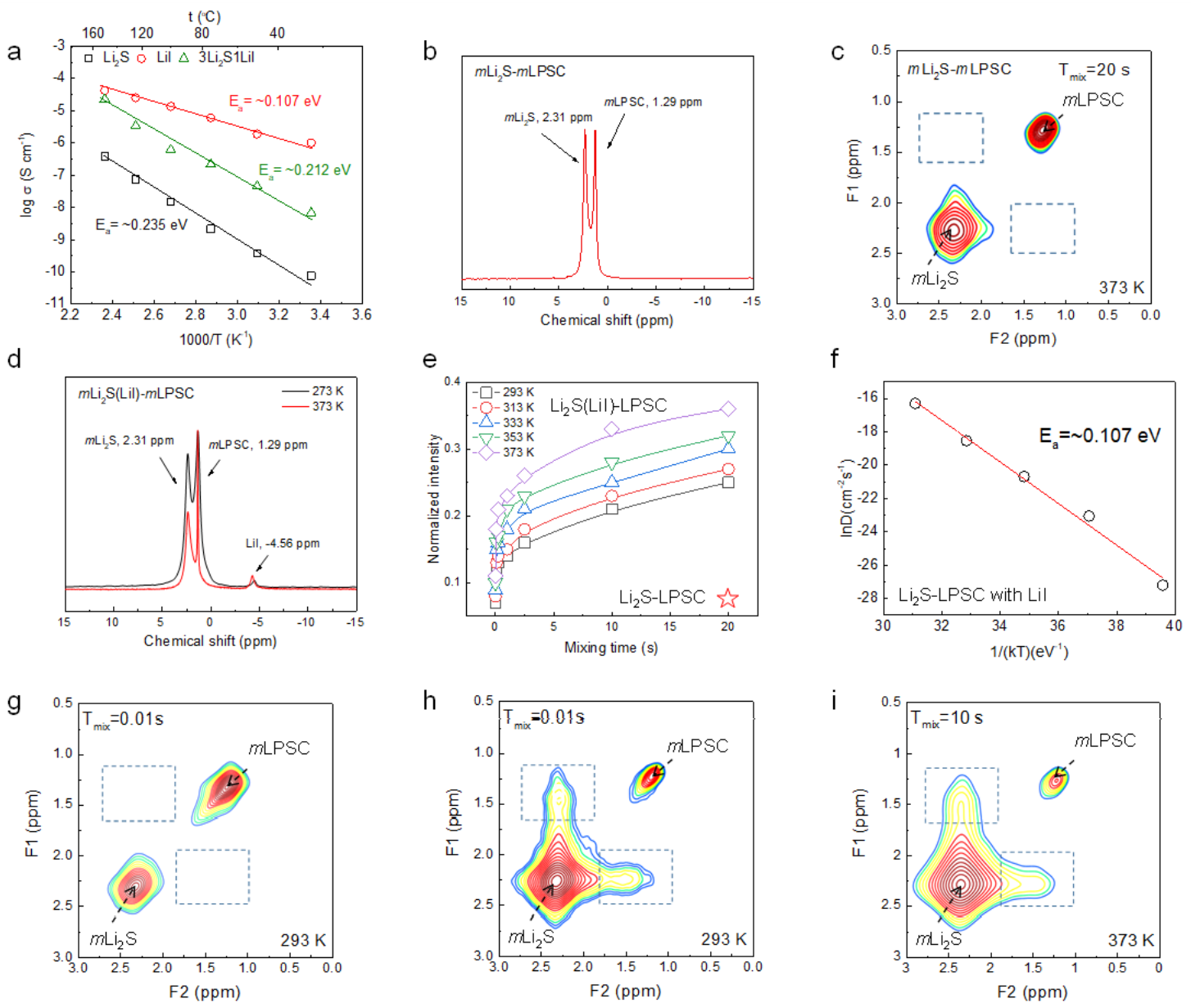


Figure 3

Conductivity of the cathodes and quantification of the charge transfer across the electrode-electrolyte interface. (a) Ionic conductivity determined by impedance spectroscopy of pellets of Li₂S, LiI and the Li₂S-LiI mixture at different temperatures. (b, c) One-dimensional (1D) ⁶Li magic angle spinning (MAS) and two-dimensional (2D) ⁶Li-⁶Li exchange (2D-EXSY) spectra of the mLi₂S-mLPSC cathode mixtures at a mixing time of 20 s, where Li₂S and LPSC are both micron-sized. No obvious off-diagonal cross-peak intensity is observed, indicating that the exchange of Li⁺ over the solid-solid LPSC-Li₂S interface is very small. (d) 1D ⁶Li MAS spectra corresponding to the mLi₂S(LiI)-mLPSC cathode mixtures at 273 and 373 K. (e) Evolution of the cross-peak intensity as a function of T_{mix} obtained from the temperature dependent 2D-EXSY measurements. (f) Temperature dependence of the diffusion coefficient obtained from fitting the data in (e) to a diffusion model described detail in reference 24. These can be fit with an Arrhenius law, yielding an activation energy (E_a) of 0.107 eV. (g-i) Two-dimensional ⁶Li-⁶Li exchange

spectra of the mixture of micron sized LPSC and Li₂S-Lil (3:1) cathodes measured at a spinning speed of 10 kHz at (g,h) 293K with mixing times of 0.01s and 10 s and at (i) 373K with a mixing time of 10 s. The spectra consist of 16 scans for each of the 32 slices, each slice incremented by 8 ms with a recycle delay of 5 s. The cross-peak at the off-diagonal positions in the dashed boxes represent diffusion of Li-ions between solid electrolyte and electrode.

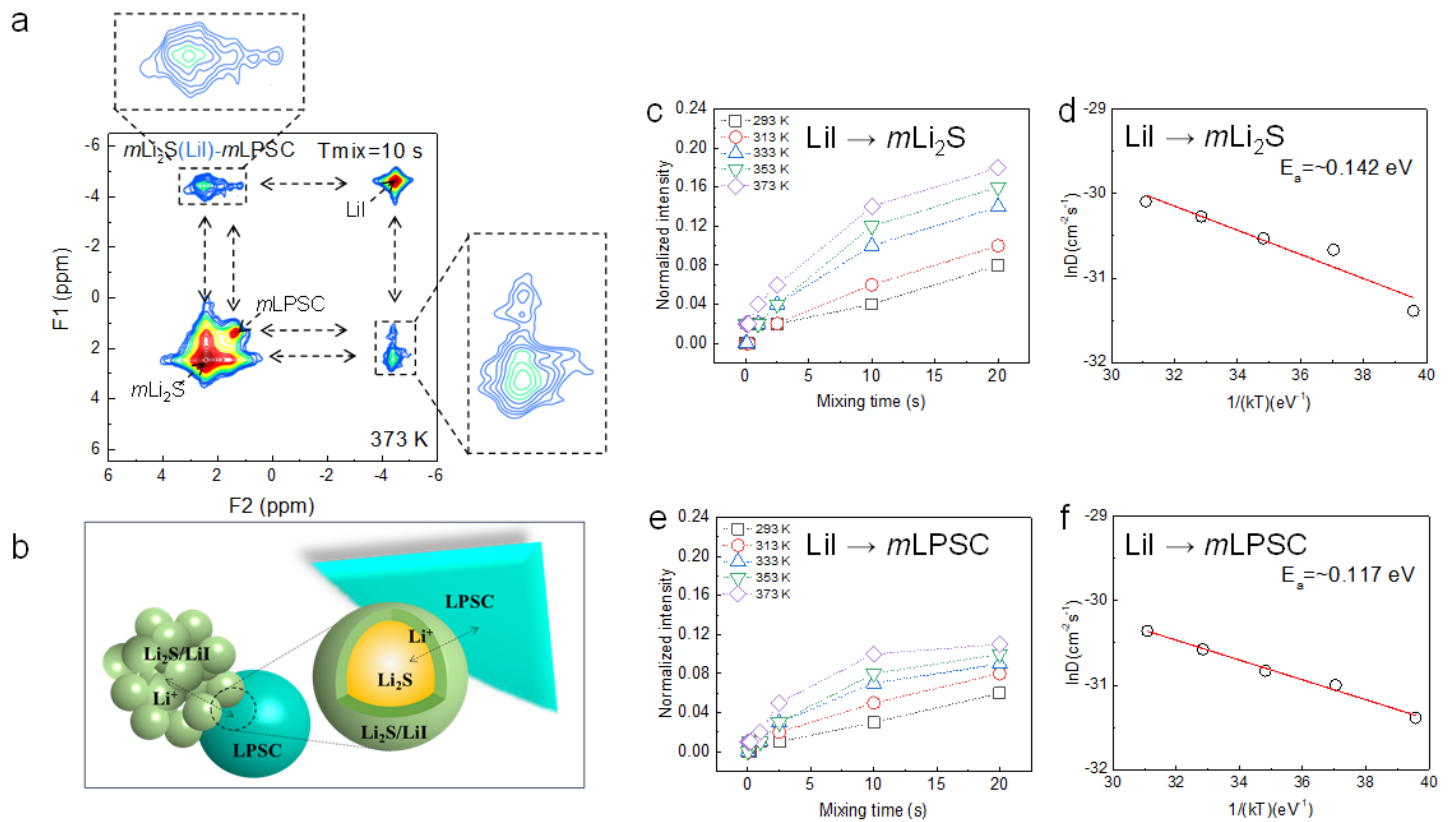


Figure 4

Mechanism for Li⁺ transport in the mLi₂S(Lil)-mLPSC-C cathodic mixtures. (a) Two-dimensional 6Li-6Li exchange spectra of the mixture of LPSC and Li₂S-Lil powders measured at spinning speed of 10 kHz at 100 °C and a mixing time of 10 s. (b) Proposed schematic mechanism for Li⁺ transport in the mLi₂S(Lil)-mLPSC-C cathodic mixtures. (c, e) Evolution of the cross-peak intensity as a function of Tmix obtained from the temperature dependent 2D-EXSY measurements. (d, f) Temperature dependence of the diffusion coefficient obtained from fitting the data in (c, e).

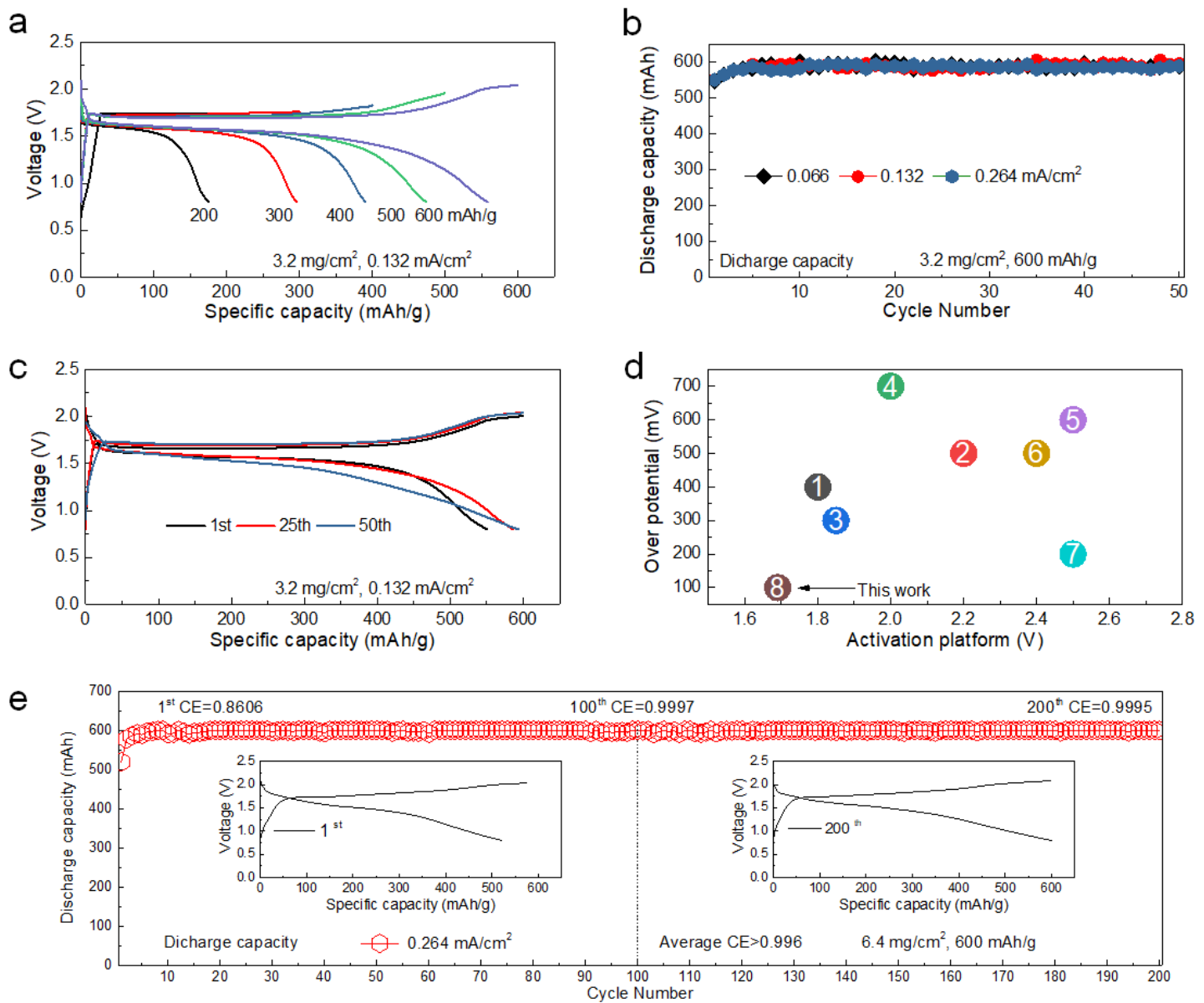


Figure 5

Electrochemical performance of mLi₂S(LiI)-mLPSC batteries. (a) Charge and discharge curves of the mLi₂S(LiI)-mLPSC-C|mLPSC|In-Li battery cycled incrementally from 200 to 600 mAh/g at a 0.132 mA/cm² current density; (b) Discharged capacity of mLi₂S(LiI)-mLPSC-C|mLPSC|In-Li battery cycled to 600 mAh/g at 0.066, 0.132 and 0.264 mA/cm² respectively; (c) 1st, 25th and 50th charge and discharge curves of mLi₂S(LiI)-mLPSC-C|mLPSC|In-Li battery cycled at 0.132 mA/cm² current density; (d) Overpotential versus average activation voltage comparing results from literature as listed in Table S1 with the present work; (e) Discharge capacity of the mLi₂S(LiI)-mLPSC-C|mLPSC|In-Li battery cycled to 600 mAh/g at 0.264 mA/cm² current density up to 200 cycles.

Supplementary Files

This is a list of supplementary files associated with this preprint. Click to download.

- [LiSNCI.docx](#)